A&A 425, 121–131 (2004)
DOI: 10.1051/0004-6361:20047104

Astronomy & Astrophysics

Geometry of the non-thermal emission in SN 1006⋆

Azimuthal variations of cosmic-ray acceleration

R. Rothenflug[1], J. Ballet[1], G. Dubner[2], E. Giacani[2], A. Decourchelle[1], and P. Ferrando[1]

[1] DSM/DAPNIA/SAp, CEA Saclay, 91191 Gif-sur-Yvette Cedex, France
e-mail: jballet@cea.fr
[2] IAFE, CC 67, Suc.28-(1428) Buenos Aires, Argentina

Received 20 January 2004 / Accepted 15 April 2004

Abstract. SN 1006 is the prototype of shell supernova remnants, in which non-thermal synchrotron emission dominates the X-ray spectrum. The non-thermal emission is due to the cosmic-ray electrons accelerated behind the blast wave. The X-ray synchrotron emission is due to the highest energy electrons, and is thus a tracer of the maximum energy electrons may reach behind a shock. We have put together all *XMM-Newton* observations to build a full map of SN 1006. The very low brightness above 2 keV in the interior indicates that the bright non-thermal limbs are polar caps rather than an equator. This implies that the ambient magnetic field runs southwest to northeast, along the Galactic plane. We used a combined VLA/Parkes radio map to anchor the spectrum at low energy, and model the spectra with synchrotron emission from a cut-off power-law electron distribution, plus a thermal component. We present radial and azimuthal profiles of the cut-off frequency. The cut-off frequency decreases steeply with radius towards the center and with position angle away from the maximum emission. The maximum energy reached by accelerated particles, as well as their number, must be higher at the bright limbs than elsewhere. This implies interesting constraints for acceleration at perpendicular shocks. Overall the *XMM-Newton* data is consistent with the model in which the magnetic field is amplified where acceleration is efficient.

Key words. acceleration of particles – magnetic fields – ISM: cosmic rays – ISM: supernova remnants – X-rays: individuals: SN 1006

1. Introduction

The current paradigm is that the bulk of the cosmic-rays (up to the "knee" at 3×10^{15} eV) are accelerated at the blast waves generated by supernova explosions in our galaxy (Blandford & Eichler 1987). Indeed supernova remnants (SNRs) are all non-thermal radio emitters, attesting of the presence of accelerated electrons at energies of 1 GeV or so in larger amounts than in the average interstellar medium. The radio emission is limb-brightened, confirming that those accelerated electrons originate at the shock.

Synchrotron emission by accelerated electrons is detected up to the X-rays in SN 1006. It dominates in the two bright limbs (northeast and southwest), whereas thermal (line) emission dominates in the center and towards the northwest and southeast (Koyama et al. 1995). The spectral index in the X-rays ($\alpha = 1.9$) is much steeper than in the radio ($\alpha = 0.6$). This is a measure of the high energy cut-off in the electron distribution, and is predicted by non-thermal emission models (e.g., Ellison et al. 2000). The comparison between the radio and X-ray emission in a number of remnants in the Galaxy (Reynolds & Keohane 1999) and the Magellanic Clouds (Hendrick & Reynolds 2001) resulted in cut-off energies between 10 and 80 TeV, assuming $B = 10\ \mu$G.

SN 1006 was also detected at TeV energies (Tanimori et al. 1998). This emission was interpreted as inverse Compton on the Cosmic Microwave Background, and the comparison between the synchrotron and inverse Compton components results in an estimate of the magnetic field strength in the remnant $B \leq 10\ \mu$G. If that is true, the radiative losses are unimportant even for electrons, and the high energy cut-off should be the same for the protons and the electrons. SN 1006 then offers an opportunity to test the theoretical predictions (Lagage & Cesarsky 1983) on the maximum energy which cosmic-rays may reach in supernova remnants.

On the other hand Berezhko et al. (2002) have proposed that the TeV emission is dominated by π_0 decay, and the magnetic field at the bright limbs could be as high as $100\ \mu$G. This is supported by the very thin filaments observed by *Chandra* (Bamba et al. 2003), whose width is probably limited by radiative losses.

Any acceleration model predicts specific radial and azimuthal variations of the X-ray synchrotron spectrum. *XMM-Newton* is ideally suited to study that, as its spatial resolution (HEW around 15″) corresponds to less than 2%

⋆ Based on observations obtained with *XMM-Newton*, an ESA science mission with instruments and contributions directly funded by ESA member states and the USA (NASA).

of the angular radius of SN 1006 (15′). Its field of view is large enough to allow full coverage with a reasonable number of pointings. *XMM-Newton* cannot compete with *Chandra* in terms of detailed spatial studies (Long et al. 2003) because of its lower spatial resolution. Our goal here is rather to present a global view of the large scale structure of the non-thermal emission in SN 1006, aiming at understanding how the initial orientation of the magnetic field affects particle acceleration. To make full use of the X-ray maps in terms of measuring the spectral cut-off, it is necessary to anchor them at lower frequency, in the radio. To that end we have built a full radio map at the best spatial resolution available.

Section 2 details where the data we have used comes from. Section 3 shows full maps of SN 1006 in several energy bands, as well as transverse profiles across the limbs and azimuthal profiles along the shock. Section 4 gives the results of the spatially resolved spectral analysis, radially and azimuthally. Section 5 analyses the results in the view of other observations and models of SN 1006.

2. Origin of the data

2.1. Radio

We wish to be able to extract the radio flux coming from any region of SN 1006, for comparison with the X-rays and spectral modeling (Sect. 4.1). For that purpose we need a radio image containing all the flux. This can be achieved from the merging of interferometric with single dish data, which allows to recover information at all spatial frequencies. The Molonglo/Parkes 843 MHz radio map (Roger et al. 1988) suited our purpose, but its spatial resolution (HPBW 64″×43″) was somewhat too low.

A new radio image was produced from the re-processing of VLA (NRAO[1]) archive data which were combined with new single dish observations.

The VLA data were originally acquired in the CnB and DnC hybrid configurations (Moffett et al. 1993) at 1370 and 1665 MHz. An interferometric image was obtained at the average frequency of 1517.5 MHz from the full database using AIPS software. Primary beam correction was applied.

Since the interferometric observations are insensitive to structure on angular scales greater than ∼20′, and the remnant is about 30′ in diameter, we observed SN 1006 with the Parkes[2] 64-m radiotelescope in order to recover information on all spatial scales. The Parkes observations were carried out in two 9 h sessions on 2002, September 1 and 2 using the Parkes Multibeam system. The correlator was centered at 1468 MHz in order to avoid strong radio interference that occurs at 1499 MHz. A second order polynomial baseline was subtracted to the data cube. An integrated moment map was produced using tasks in the data reduction package *MIRIAD*.

[1] The National Radio Astronomy Observatory is a facility of the National Science Foundation operated under a cooperative agreement by Associated Universities Inc.

[2] The Parkes telescope is part of the Australia Telescope which is funded by the Commonwealth of Australia for operation as a National Facility managed by CSIRO.

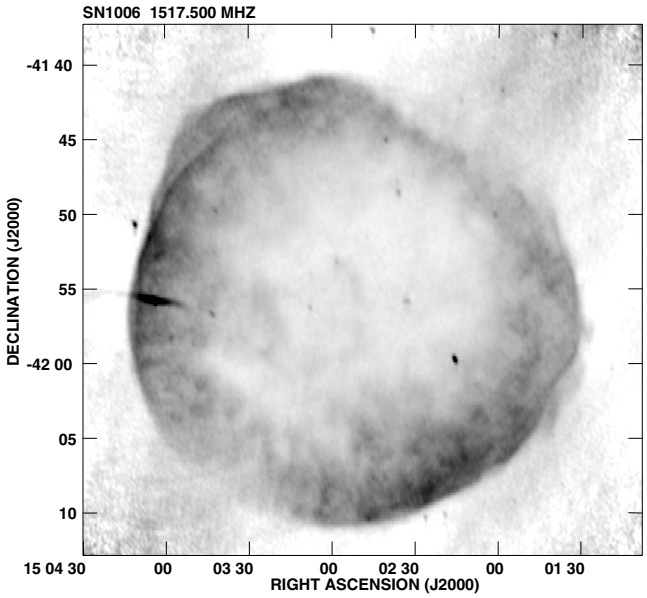

Fig. 1. Grey-scale image of SN 1006 at 1517.5 MHz. The grey-scale varies linearly between 0.2 and 6.5 mJy/beam. The HPBW is 22.8″× 12.8″. The bright elongated source near (α, δ) = (15 04 04, –41 55 47) is a background radio galaxy (Reynolds & Gilmore 1986). The diffuse radio emission seen at the southeast and northwest corners is an instrumental spurious feature.

Units were changed assuming a Gaussian beam of 14.4′ which gives the conversion factor Jy/K = 1.5.

Interferometric and single-dish data were combined in the *uv* plane using the task *immerge* in *MIRIAD*, which merges the two sets of data in the Fourier plane to form an image accurate up to the resolution of the interferometric image. The final image has an angular resolution of 22.8″ × 12.8″ and an rms noise of 0.1 mJy/beam. The total recovered flux after background correction is 15.2 Jy. The resulting image is shown in Fig. 1.

2.2. X-ray

Six observations of SN 1006 exist in the *XMM-Newton* archive (Table 1). They were all obtained with the Medium filter. Results were already reported on one of those (Vink et al. 2003), focusing on the thermal emission. Together those observations cover the whole remnant, allowing to build a full X-ray map. The "good" columns in Table 1 indicate the exposure time left after flare screening. 0126_0111090301 (southwest) was screened with relaxed criteria (otherwise nothing would have been left). This is acceptable because the southwest limb is much brighter than the background. The total exposure map is shown in Fig. 2 (bottom right). It is essentially the same for all the maps shown here (vignetting is energy dependent mostly above 5 keV). The coverage is good and homogeneous in the north, but much shallower in the south (particularly the southwest limb).

The EPIC PN exposure time in the southwest (where the covering is worst) is 0. This means that including PN data would have added time mostly where the exposure was largest already. The cost would have been a less precise exposure

Table 1. List of *XMM-Newton* observations used in that paper.

Revolution_ObsID	Observation date	Pointing direction (decimal degrees)			MOS exp. (ks)		PN exp. (ks)	
		RA (J2000)	Dec (J2000)	Pos. angle	Total	Good	Total	Good
0126_0111090301 (SW)	2000 August 17	225.6082	–42.1542	289.30	5.01	2.44	0.92	0.00
0128_0111090101 (NE)	2000 August 20	225.9759	–41.8071	290.22	7.43	7.43	2.97	2.97
0305_0111090601 (SE)	2001 August 08	225.8932	–42.0396	286.28	15.77	5.95	10.46	5.95
0306_0077340101 (NW)	2001 August 10	225.4717	–41.8425	296.11	64.85	33.41	56.33	33.41
0306_0077340201 (NE)	2001 August 11	226.0507	–41.8978	276.32	57.18	10.18	44.57	10.18
0674_0143980201 (NE)	2003 August 14	225.9115	–41.8269	286.04	30.08	13.62	23.35	13.33

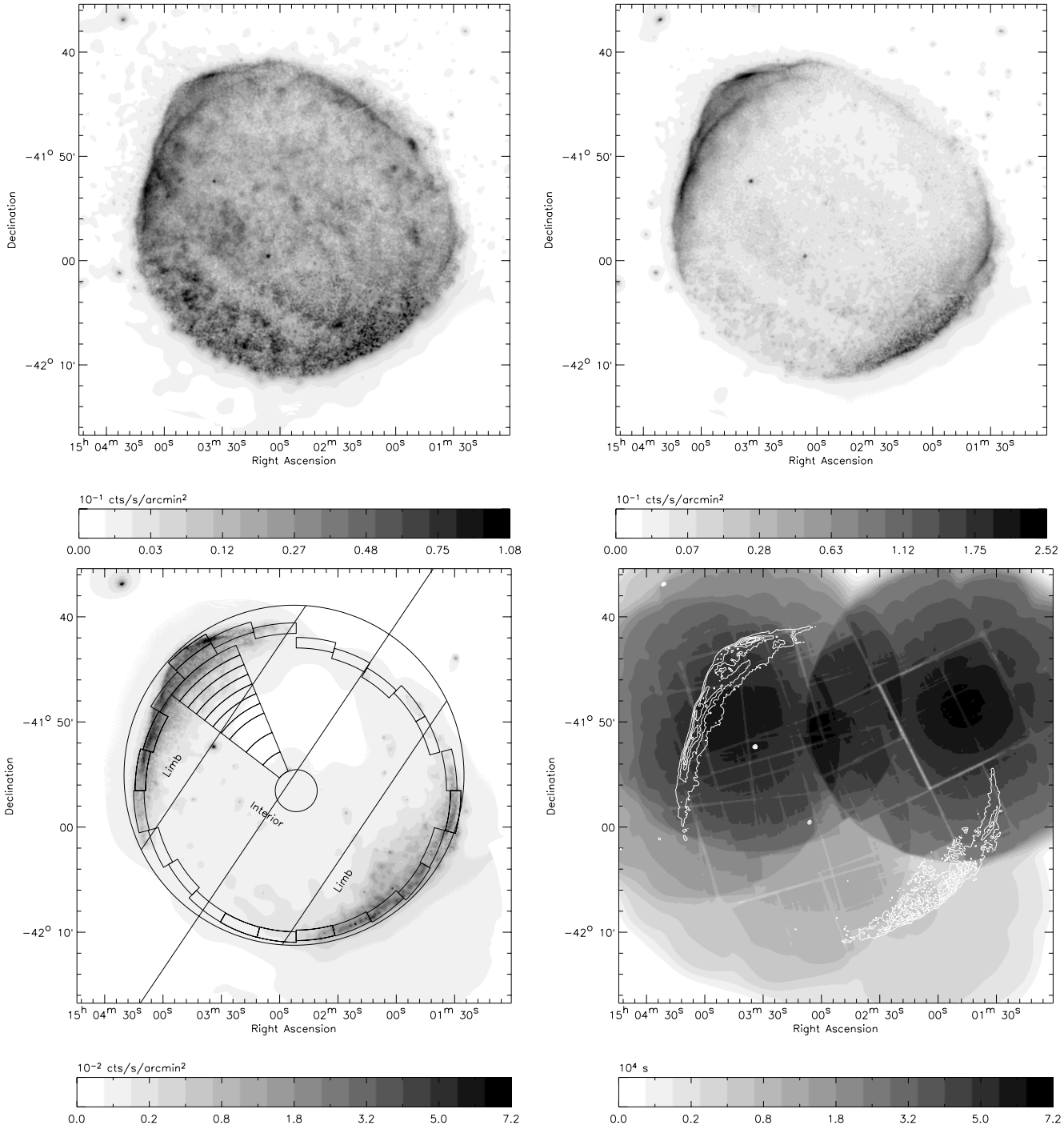

Fig. 2. EPIC MOS images in the 0.5 to 0.8 keV (oxygen lines, *top left*), 0.8 to 2 keV (*top right*) and 2 to 4.5 keV (*bottom left*) bands. The scale is square root to show better the weak features. The symmetry axis used in Fig. 5, the partition of the emission between interior and limbs (Sect. 3.2), and the regions for the spectral analysis (Sect. 4) are drawn. *Bottom right*: associated exposure map (in units of equivalent time for one MOS). The scale is square root to show better the weak features. The contours of the 0.8 to 2 keV image are overlaid.

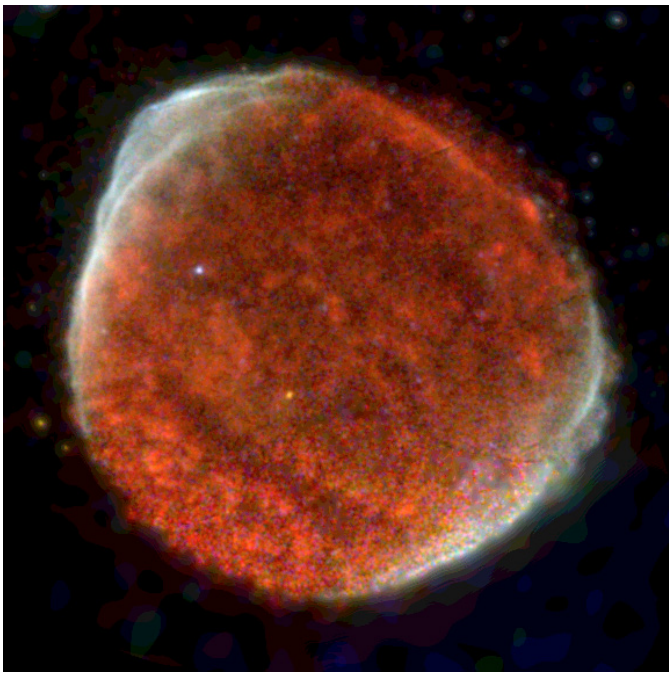

Fig. 3. Three-color image of SN 1006. The red, green and blue channels are 0.5 to 0.8 keV (oxygen lines), 0.8 to 2 keV and 2 to 4.5 keV, respectively. The areas dominated by non-thermal emission appear white (equally bright in all three bands). The areas dominated by the thermal emission appear red (softer).

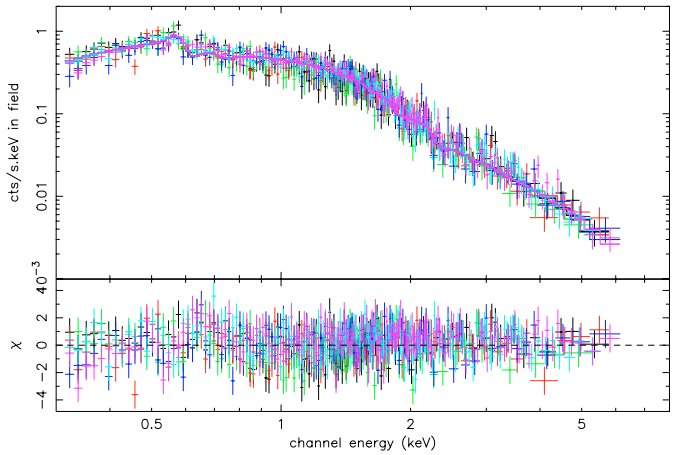

Fig. 4. EPIC MOS spectra extracted from a single region (east, PA = 75 to 90°). Six spectra are overplotted, corresponding to both MOS instruments and three observations obtained at different epochs: 0128_0111090101, 0305_0111090601, 0674_0143980201 (Table 1). The spectra are essentially identical, illustrating the good stability of the instrument over three years. The model is the VPSHOCK + SRCUT XSPEC model used in Sect. 4.

correction because the ratio between PN and MOS effective areas depends on energy. For that reason we decided to keep a homogeneous data set using EPIC-MOS (Turner et al. 2001) only. The data was processed using XMM SAS 5.4.1. The *evigweight* procedure was used to facilitate the spectral analysis, but the imaging analysis was carried out via exposure maps.

This data offers the same spatial resolution as *ROSAT* HRI (Winkler & Long 1997) but with energy resolution similar to that of *ASCA* (Koyama et al. 1995). It is better in both respects than *ROSAT* PSPC (Willingale et al. 1996). The *XMM-Newton* observation is also deeper than that of *ROSAT* and *ASCA* except in the south. It has comparable depth as the *Chandra* observation (Long et al. 2003) which did not cover the southwest at all.

3. Imaging

3.1. Maps

The instrumental background was subtracted using the reference event lists compiled by Read & Ponman (2003). The background maps were normalised on the count rate above 10 keV (the EPIC MOS count rate from SN 1006 above 10 keV is negligible). The mosaics were built in counts, and exposure maps built in parallel. Adaptive smoothing (to a signal to noise ratio of 5) was applied at that stage (using the XMM SAS task *asmooth*). The same smoothing was applied to the exposure map. The final maps (Fig. 2) were obtained by dividing the smoothed image by the smoothed exposure map. It is obvious in the images that the southwest is more smoothed than the northeast. This is not due to any intrinsic difference between both limbs, but to the very short exposure time on the southwest limb, resulting in more smoothing to get the same signal to noise ratio. The apparent extension beyond the blast wave is also the result of the smoothing procedure.

Because the reference background contains an astrophysical background which is not in general the same as that around SN 1006, we have subtracted a constant (positive or negative) to the final maps (in each band) in order that the flux outside SN 1006 be 0 (i.e. we assume that the background does not vary over SN 1006). The remaining weak background outside SN 1006 to the southwest (best seen above 2 keV) is due to the imperfect flare screening there.

One difference can already be stated by comparing the "non-thermal" X-ray map above 2 keV (Fig. 2, bottom left) with the radio map (Fig. 1). The maximum X-ray brightness (J2000) is in the filament around $(\alpha, \delta) = (15\ 03\ 37.2, -41\ 42\ 18)$ which is relatively faint in the radio. By contrast, the radio brightness peaks around $(\alpha, \delta) = (15\ 04\ 05.5, -41\ 51\ 40)$, more than 10′ away along the shock front.

Figure 3 uses the three bands together to illustrate again the dual nature of SN 1006: pixels are either red (oxygen line, thermal) or white (all bands, non-thermal). No part of SN 1006 is blue (very hard) or green (dominated by Ne or Si lines). For that figure we applied the same smoothing (optimised on the oxygen band) to all three bands.

3.2. Profiles

SN 1006 has a simple bipolar morphology which makes it the best candidate for understanding the acceleration geometry in physical terms. The most natural reason for that morphology is that the pre-supernova orientation of the magnetic field created a preferred axis. The radio observations were interpreted as being due to the magnetic field being initially oriented from southeast to northwest, so that the bright limbs correspond to

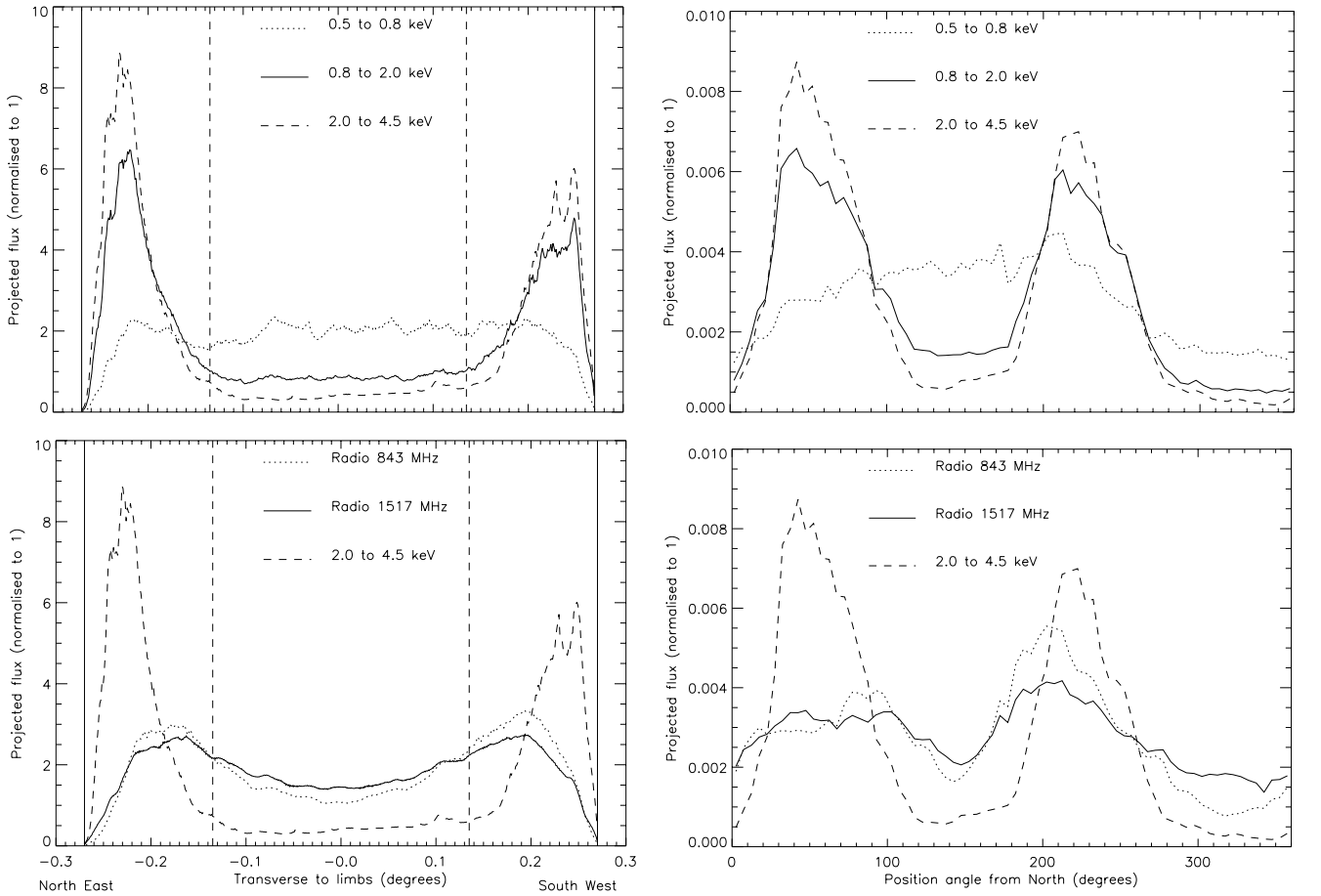

Fig. 5. *Top*: profiles of X-ray flux in several energy bands. *Bottom*: profiles of radio flux at two frequencies. The 843 MHz image is from Roger et al. (1988). The X-ray profiles in the hard band (where thermal emission is negligible) are reported for easy comparison. *Left*: projection transverse to the apparent symmetry axis of SN 1006 (PA = −34° from north, Roger et al. 1988). The dashed line shows the limit between the "interior" and the "limbs" used in Sect. 3.2. *Right*: azimuthal (counterclockwise) profiles integrated over angular radius from 0 to 0.27°.

the magnetic "equator" (Reynolds 1996). That geometry definitely predicts that the emission from the front and back sides (projected near the center of the remnant) should be approximately the same as that of the limbs.

An annoying point which has to be decided before proceeding further is where to place the center of the remnant. SN 1006 is not so symmetric when looked at in detail, so different assumptions lead to significantly different results. In this section we choose the center which allows to enclose all emission in a circle of minimum radius. It is depicted in Fig. 2 (bottom left). The center (J2000) is $(\alpha, \delta) = (15\ 02\ 52.8, -41\ 58\ 48)$ and the angular radius is 0.27°.

To quantify the bipolarity, Fulbright & Reynolds (1990) have used the ratio A of maximum to minimum intensity along the shock. Willingale et al. (1996) have used a deprojection algorithm assuming a spherical emissivity distribution in 15° angular sectors. Here we introduce a somewhat different geometrical quantity. We integrate the X-ray map along the apparent symmetry axis (Fig. 2, bottom left) to build a profile transverse to the bright limbs. We show in Appendix A that in any axisymmetric model, whatever the angle between the magnetic field and the line of sight, the ratio $\mathcal{R}_{\pi/3}$ of the flux in the interior half of the SNR to that in the limbs (Fig. 5, left) must be at least 0.5 (because the equator must also be present at the front and the back).

In the radio (Fig. 5, bottom left), $\mathcal{R}_{\pi/3}$ is about 0.7. But in the X-rays, $\mathcal{R}_{\pi/3}$ is observed to be $F_{\rm in}/F_{\rm out} = 0.300 \pm 0.014$ (0.8 to 2.0 keV), and 0.127 ± 0.074 (2.0 to 4.5 keV). The thermal emission (dominant in the 0.5 to 0.8 keV band profile of Fig. 5, top left) is much more uniform and contributes at some level at higher energy, so the observed ratios should be taken as upper limits for the non-thermal emission itself. Those values are clearly incompatible with an equatorial model (there is no room for strong X-ray emission at the front or the back).

We conclude that the most likely explanation for the bright limbs is that they are polar caps instead of an equatorial belt, and that acceleration is proceeding preferentially where the magnetic field is parallel to the shock speed. The same conclusion was reached by Willingale et al. (1996) using *ROSAT* PSPC. This geometry is preferred by most theoretical models (e.g., Berezhko et al. 2002). The magnetic field is then oriented along the Galactic plane (southwest–northeast).

Beyond that, Fig. 5 (bottom) shows clearly that the non-thermal X-rays are much more contrasted than the radio emission. This is the origin of the strong spectral variations which will be discussed in Sect. 4.2. Figure 5 (top right) shows that

the thermal emission (0.5 to 0.8 keV band) is rather uniform, but with a significant minimum toward the northwest. This is paradoxical, because that direction is, according to Hα observations (Winkler et al. 2003), where the density in the ambient medium is largest. If it was due to additional extinction there, the column density would need to be about 1.4×10^{21} cm^{-2} to reduce the flux by a factor 2 (as observed) in that band. This is much larger than the total column density derived by Dubner et al. (2002), so extinction is unlikely to be the reason. The minimum of the non-thermal emission (both in X-rays and in the radio) is also toward the northwest.

4. Spectral modeling

4.1. Procedure

XMM-Newton offers the possibility to study spectral variations at a spatial resolution allowing to resolve the bright limbs. Dyer et al. (2001) have characterized the broad-band global spectrum of SN 1006 in terms of a power-law spectrum (cut-off at high frequency) plus a thermal spectrum. We used the same kind of approach, but locally. To characterise the broad-band synchrotron emission, the X-ray data need to be fitted together with the radio data, which gives the spectral index and the normalisation of the power-law part. The combined VLA/Parkes radio data (Sect. 2.1) ensures that no flux is lost at short spatial frequencies. It has lower spatial resolution than *XMM-Newton*, but the X-ray data is limited by statistics in the south anyway.

For defining regions for the spectral analysis we chose to use the center proposed by Reynolds & Gilmore (1986) whose J2000 coordinates are $(\alpha, \delta) = (15\ 02\ 51.7, -41\ 56\ 33)$, about 1.5′ away from the center we used in Sect. 3.2. The fact that the results (Sect. 4.2) are qualitatively similar to those of Sect. 3.2 indicates that they are robust.

We extracted spectra in a number of regions just inside the rim of SN 1006, every 15° in azimuth. The width of the regions (1′) was chosen in keeping with the resolution of the radio map and the statistics in the X-ray data. To locate the shock front, the radial profile in the 0.5 to 1.2 keV band (which offers the best contrast between SN 1006 and the background) was built at each azimuth. The outer radius was set at the point where the signal was one half of the maximum. The resulting regions are shown in Fig. 2 (bottom left). They are about 1′ wide except close to the center (2′), and 30° broad except the first two (15°) and the central one (full disk).

For each region, each instrument and each observation, the instrumental background was derived for the same detector region from the event lists compiled by Read & Ponman (2003) as in Sect. 3.1. Each background spectrum was corrected for the background exposure map (sources were excised to build the background event lists, so the exposure is not uniform). The main contribution to this background comes from cosmic ray particles whose contribution is slightly variable in time. The ratio of the counting rate between 10 and 12 keV (where the sensitivity to X-rays is very low) was computed for the whole field of view in each observation: this ratio was then used to normalise each background spectrum with respect to the corresponding observation spectrum. Another contribution to the background comes from the soft X-ray background which varies from place to place in the sky: a reference X-ray background spectrum was derived outside SN 1006, analysed in the same way as the SN 1006 spectra and added to the instrumental background to obtain the total background to be subtracted to the observation spectrum in a given region (see Arnaud et al. 2002, for a complete description of this method). For each region, we extracted at least 2 and up to 6 spectra, since the different observations overlap in the sky. Examples of X-ray spectra are shown in Figs. 4 and 6.

A band of diffuse radio emission is observed running southeast to northwest in the radio map (Fig. 1). This is a spurious feature of instrumental origin and was taken into account by subtracting from the radio signal in the azimuthal regions the signal measured in a region at the same azimuth but beyond the blast wave. Because this procedure is applicable only very close to the shock, we did not apply it to the radial regions. The residual radio emission beyond the shock toward the northeast limb is not very large anyway.

Dubner et al. (2002) have mapped the variations in interstellar absorption towards SN 1006 and shown that it was rather uniform. In our modeling we fixed it to the average value $N_{\rm H} = 7 \times 10^{20}$ cm^{-2}.

Each spectrum is reasonably well fitted with a 2-component model in XSPEC: synchrotron emission from a cut-off electron power law (SRCUT) plus thermal emission from a plasma out of ionisation equilibrium behind a shock (VPSHOCK) with variable abundances. The radio flux was extracted from the radio map in each region. The radio spectral index was fixed to 0.6 (Dyer et al. 2001). The cut-off frequency was the only free parameter of the synchrotron component. It is related to the cut-off energy on the electrons by

$$\nu_{\rm cut}\,({\rm eV}) \;\simeq\; 0.02\, B\,(\mu{\rm G})\, E^2_{\rm cut}\,({\rm TeV}). \qquad (1)$$

It is very possible that the spectral index varies over the remnant, but we have chosen to ignore it for two reasons:

1. except in the northeast bright limb, there is not enough statistics in the X-ray spectra to constrain separately the slope and the cut-off frequency. This is either because of the very short exposure time (southwest limb) or because the non-thermal X-ray emission is intrinsically weak (southeast and northwest). We preferred applying the same method to the whole data set;
2. the most likely reason for a varying spectral index is the dynamic effect of the accelerated particles themselves (Reynolds & Ellison 1992). However this results in a concave spectrum (e.g. Baring et al. 1999) which would not be well modeled by the SRCUT model anyway.

The thermal emission is compatible with the earlier *ASCA* results. The individual parameters of the VPSHOCK component are little constrained, but we checked that this does not affect the cut-off frequency measure. A detailed analysis of the thermal emission deserves a separate paper.

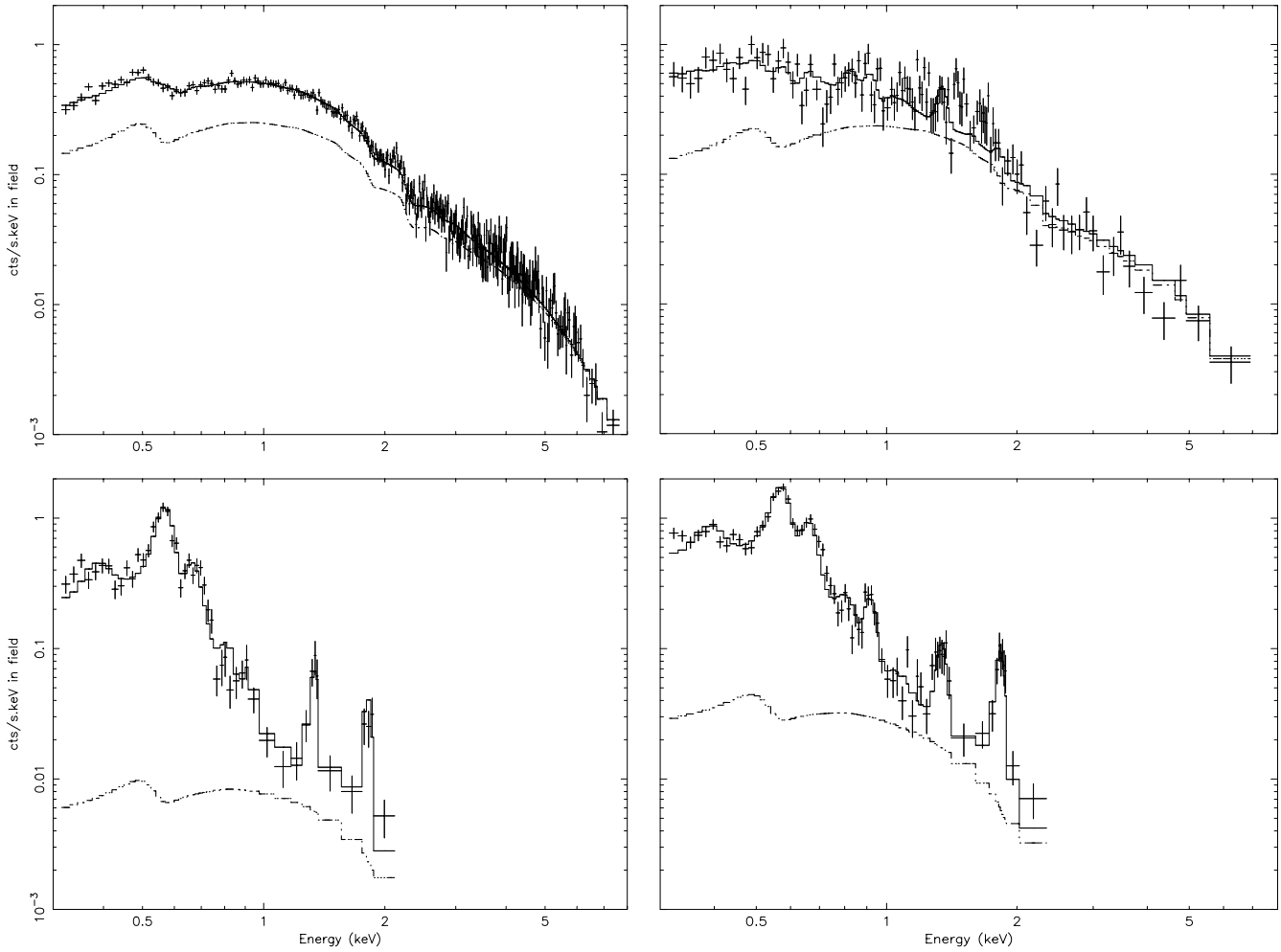

Fig. 6. Examples of EPIC MOS spectra extracted from several regions over the remnant, with the best spectral fit (Sect. 4.1). The synchrotron component of the model is overplotted (dotted curve). Thermal emission makes up the difference. The data is the average of both MOS detectors over all the observations covering the region. *Top left*: bright X-ray filament (northeast, PA = 30 to 45°). *Top right*: bright X-ray filament (southwest, PA = 210 to 225°). *Bottom left*: behind the shock in the southeast (PA = 135 to 150°). *Bottom right*: near the center of the remnant.

4.2. Synchrotron cut-off frequency

The azimuthal variations of the break frequency are shown in Fig. 7 (left). Numerically, if $B \simeq 10\,\mu$G, the cut-off energy at the bright limb is ≃200 TeV from Eq. (1). If $B \simeq 100\,\mu$G, $E_{\rm cut} \simeq$ 60 TeV. The radial variations are shown in Fig. 7 (right). This is directly the observed (2-D) structure. We did not attempt to deconvolve it to reach the 3-D structure.

Bamba et al. (2003) applied the same SRCUT + thermal model to *Chandra* data of the northeast rim, with two important differences. First they do not fix the normalisation of the non-thermal component on radio data (there is no adequate radio map at their spatial resolution), but let it free. This means that their $\nu_{\rm cut}$ is sensitive to the local curvature, whereas ours is sensitive to the X to radio ratio. Second they let $N_{\rm H}$ free (and find values around 1.3×10^{21} cm^{-2}, much larger than indicated by the HI observations (Dubner et al. 2002). In spite of those differences, their results are strikingly similar to ours. They also find a very large $\nu_{\rm cut}$ in the outermost northeast filament (PA = 30 to 45°), and values around 2 keV in the rest of the northeast limb.

Because of the very simple spectral model that we used, the cut-off frequencies that we get should not be interpreted too literally. In particular, they depend rather strongly on the particular radio slope that we have used. Actually what we see are mostly variations of the X-ray to radio ratio. This is a quantity that is directly comparable to any model. Therefore we have converted back the cut-off frequency to the ratio between X-ray (1 keV) and radio (1 GHz) brightness in the non-thermal component (Fig. 8). This could not be done directly from the images because of the strong contribution of the thermal emission outside the bright limbs. Figure 8 overlays the same ratio obtained from the MOST + Parkes radio map (Roger et al. 1988). Qualitatively, a very similar azimuthal modulation is obtained with both radio maps, even though significant differences exist (most conspicuously between both bright limbs). Figure 8 also illustrates how the background subtraction in the radio map

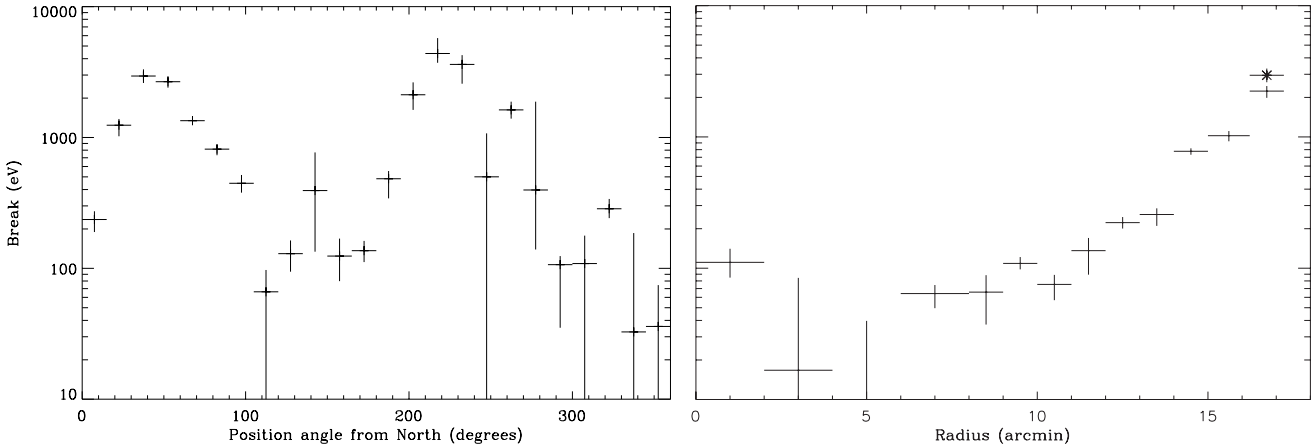

Fig. 7. Variations of the cut-off frequency of the synchrotron component of the model. *Left*: azimuthal variation close to the shock. *Right*: radial variation in an angular sector toward the northeast limb. No background subtraction has been applied to the radio map in the radial profile. For comparison, the result with background subtraction (as in the azimuthal profile) in the outermost region is shown with an asterisk. The azimuthal and radial regions are shown in Fig. 2, bottom left.

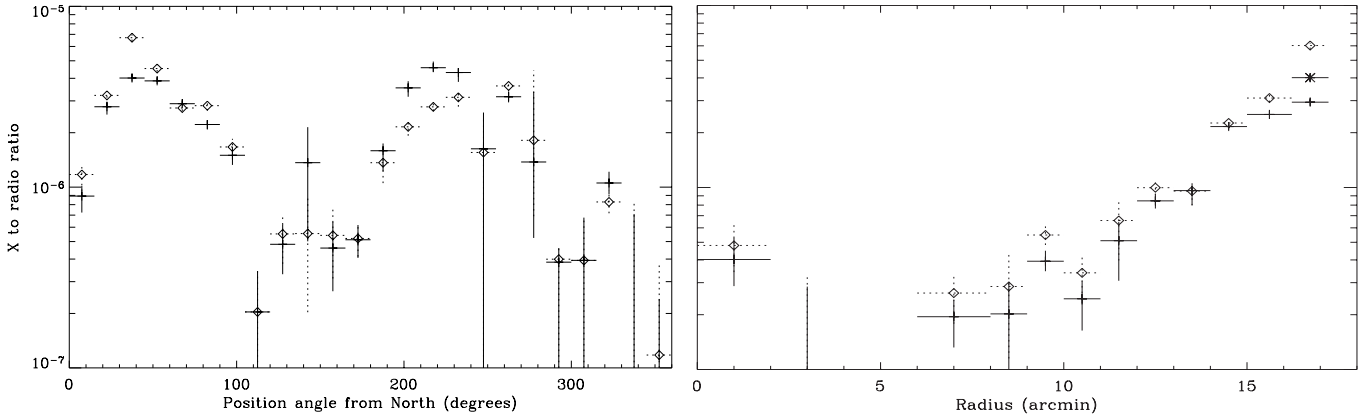

Fig. 8. Ratio of the unabsorbed X-ray brightness at 1 keV to the radio brightness at 1 GHz, in the same regions as Fig. 7. For a pure $\nu^{-0.6}$ power law this would be 9.33×10^{-6}. The simple crosses correspond to the profiles of Fig. 7, obtained with the new radio map (Sect. 2.1). The diamonds were obtained using the radio map of Roger et al. (1988). In the radial profile (*right*) the simple crosses were obtained without any background subtraction. The asterisk shows the result close to the shock with background subtraction (as in the azimuthal profile). The differences illustrate the uncertainties which are still present.

affects the results. It does not qualitatively change the conclusions either.

The azimuthal variations are very strong, much stronger than predicted in the escape model of Reynolds (1998) which Dyer et al. (2001) used (which was an equatorial model incompatible with the geometrical test of Sect. 3.2 anyway). The results imply that either B or $E_{\rm cut}$ (or both) is much larger at the bright limbs. The radial profile shows a very steep decline towards the center, which is again incompatible with the simple model in which the bright limbs are the edge brightened part of an equatorial belt (it should have the same spectrum in projection at the remnant's center). There is no indication that the X to radio ratio at the center is larger than at the southeast or northwest edges. This confirms the result of Sect. 3.2 and favors a model where the symmetry axis is southwest to northeast.

5. Discussion

5.1. The equatorial model

Fulbright & Reynolds (1990) had argued from statistical arguments (absence of center-filled SNRs) that the barrel-shaped radio SNRs were more likely equatorial (symmetry axis along the bright limbs) than polar (symmetry axis across the bright limbs). In the particular case of SN 1006, the best visual symmetry axis on the sky runs southeast to northwest (see e.g. Fig. 2, top right). On that basis, Reynolds (1996) and Dyer et al. (2001) have proposed a model in which the asymmetry in SN 1006 is due solely to a large scale magnetic field aligned southeast to northwest and inclined at 60° with respect to the line of sight, whereas the cosmic-rays are accelerated identically everywhere (up to a maximum energy

limited by escape, independent of the magnetic field orientation). In their model, the maximum synchrotron emissivity is reached where the magnetic field is most compressed, i.e. where it is "perpendicular" (to the shock normal), forming a limb-brightened equatorial belt. Assuming that the TeV emission detected by *CANGAROO* (Tanimori et al. 1998) was Inverse Compton emission, the magnetic field behind the shock had to be $\simeq$10 μG. They fitted the global spectrum of SN 006 with that escape model and concluded that $E_{\rm cut} \simeq 30$ TeV. This is particularly important for cosmic-ray acceleration, because it is too low to explain the "knee" in the cosmic-ray spectrum above 10^{15} eV, whereas at that magnetic field synchrotron losses are not very strong and electrons should have the same maximum energy as protons. The *Chandra* data on the northeast limb (Long et al. 2003) was interpreted in that framework. The very sharp rise of the X-ray emission at the shock puts stringent constraints on the model, implying that the magnetic field is somehow amplified at the shock.

On the other hand, the azimuthal variations of the radio map alone are already incompatible with that model in its simplest form (Fulbright & Reynolds 1990). Some variation of the acceleration efficiency is required, so that it is larger at the bright limbs. The radio polarisation measurements (Reynolds & Gilmore 1993) indicating that the magnetic field, although largely disordered, is predominantly radial everywhere, are also somewhat at odds with the model.

The equatorial model does predict variations in the cut-off frequency due to the variations of the magnetic compression at the shock and behind, as a function of the angle between the magnetic field and the shock normal. But the amplitude of the predicted variations, accounting for projection along the line of sight and integration in relatively large regions like ours, are no more than a factor of two between pole and equator, much less than the factor 10 or more that we observe (Fig. 7).

We conclude that the equatorial model cannot account for the observed properties of the synchrotron emission in SN 1006. It predicts an equatorial bar which is incompatible with the X-ray profile (Fig. 5, top left), and too small variations of the cut-off frequency. This conclusion is consistent with the spatially resolved ASCA data analysed by Dyer et al. (2004).

5.2. The polar cap model

The other simple alternative is that the bright limbs are polar caps. Indeed the diffusive shock acceleration injects particles more easily at parallel shocks (Ellison et al. 1995; Völk et al. 2003) and therefore predicts a larger density of accelerated particles at the poles.

In the polar cap geometry, the transverse profiles of X-ray emission (Fig. 5, top left) and the radial profile of cut-off frequency (Fig. 7, right) become very natural. In the Sedov model considered by Reynolds (1998), the expansion results in a decrease of the magnetic field behind the shock, associated to adiabatic cooling of the accelerated particles. Both effects combined can easily account for the disappearance of the X-ray emission on the relatively large scales considered here (2′), and also for the faster decrease at higher energy.

In the polar cap model, the ordered magnetic field is not amplified by compression at the limbs. If the turbulent B is not larger (as required if the TeV emission is Inverse Compton), then the magnetic field at the equator just downstream will be larger than at the limbs. From Eq. (1) and the observed ratio of cut-off frequencies (>10), the cut-off energy of the electrons has to be at least 3 or 4 times larger at the limbs. This is not very natural in acceleration theory (Ellison et al. 1995) whereby the acceleration rate (contrary to injection efficiency) tends to be larger at perpendicular shocks. If we assume the compressed interstellar field toward the southeast and northwest to be about 10 μG, the observed $\nu_{\rm cut}$ results in $E_{\rm cut} \simeq 25$ TeV. At that B and $E_{\rm cut}$ radiative losses are not an issue so this should be the maximum energy of the protons as well.

A specific model was recently proposed (Berezhko et al. 2002, 2003) whereby the TeV emission would be due to hadrons (π_0 decay) and the magnetic field would be amplified by the accelerated particles at the shock to reach 100 μG or so downstream. In that case the electrons are limited by synchrotron losses at the bright limbs. For a reasonable ordered magnetic field (<10 μG) this is at odds with the polarisation measurements (Reynolds & Gilmore 1993) which require that 20% of the magnetic energy be in the ordered field. However it explains naturally why the X-ray emission decreases as sharply downstream as observed by *Chandra* (20″ scale height, Bamba et al. 2003). The precursor should have a very similar scale height upstream. This is compatible with the *Chandra* data, as shown by Berezhko et al. (2003). Bamba et al. (2003) reported a much smaller scale height upstream, but this was based on the mistaken assumption that there should be no emissivity jump at the shock.

Berezhko et al. (2002) argue that the bright limbs are polar caps where the magnetic field (far upstream) is parallel to the shock speed. This is more in keeping with what we observe. After the amplification, the magnetic field is entirely turbulent, so its originally radial character has been lost. Nevertheless the amplification process may start only where the amount of energy channeled into the particles is large enough, and this probably never happened near the magnetic equator (Völk et al. 2003).

That model also implies that the cut-off energy of protons (which suffer no losses) is much larger than that of electrons. So in that case, even though the B term in Eq. (1) is probably larger at the bright limbs, it is still true that $E_{\rm cut}$ (of the protons) must be considerably larger there than in the fainter areas.

The turbulence level (generated by the particles themselves) is probably lower at the equator (because the density of accelerated particles is lower there). However Jokipii (1987) argued that the diffusion coefficient perpendicular to the field (across the shock) is actually smaller when turbulence is weaker, so that acceleration proceeds faster! Reynolds (1998) described several processes which limit the maximum energy of accelerated particles. The only one which may explain the very small $E_{\rm cut}$ toward the southeast and northwest is escape. Indeed if magnetic turbulence is weak the parallel diffusion coefficient can get quite large so that particles may escape along the field lines (tangentially to the shock) which get away from the shock in spherical symmetry.

The diffusive shock acceleration model limited by radiative losses predicts a maximum energy of the electrons inversely proportional to $\sqrt{B}$, so that the resulting cut-off frequency does not depend on B. To estimate it we follow the same line of reasoning and notations as Reynolds (1998) but with different initial assumptions. We assume that $\boldsymbol{B}$ is fully turbulent and isotropic just upstream of the gas shock, in the region where the streaming instability occurs, and that the mean free path is equal to the Larmor radius. The diffusion coefficient is $\kappa = Ec/(3eB)$. Then $\kappa_2 = \kappa_1/r_B$, where the indices 1 and 2 are for upstream and downstream, respectively. $r_B = B_2/B_1 = \sqrt{(1+2r^2)/3}$, where r is the compression ratio at the gas shock. In models in which a sizable fraction of the available energy is diverted to the cosmic-rays, this may be smaller than 4 (Berezhko & Völk 1997). This compression ratio applies (rather than the full one, larger than 4) because in a radiatively limited context electrons stop being accelerated at energies much smaller than that of ions, so they never reach far upstream from the gas shock. The acceleration time to energy E is

$$\tau_{\rm acc} = \frac{c\,E}{e\,B_1\,u_{\rm sh}^2}\;\frac{r}{r-1}\;\left(1+\frac{r}{r_B}\right) \tag{2}$$

where $u_{\rm sh}$ is the shock speed. In the limit of large B (negligible inverse Compton), the effective field for radiative losses is

$$\left\langle B_{\rm eff}^2\right\rangle = B_1^2\;\frac{r_B\,(1+r\,r_B)}{r+r_B}. \tag{3}$$

The maximum energy is then

$$E_{\rm m1} = 0.319\;\frac{u_8}{\sqrt{B_1}}\;\sqrt{\frac{r-1}{r\,(1+r\,r_B)}}\;\;{\rm erg} \tag{4}$$

where u_8 is the shock speed in units of 1000 km s^{-1}. The cut-off frequency is finally

$$\nu_{\rm m1} = 0.767\;u_8^2\;\frac{(r-1)\,r_B}{r\,(1+r\,r_B)}\;\;\;{\rm keV}. \tag{5}$$

The fractional term is a weakly decreasing function of r which peaks at 0.2 around $r = 2.5$ and is 0.174 for $r = 4$. For $r = 4$ and $u_{\rm sh} = 2900$ km s^{-1} taken from optical observations in the northwest (Ghavamian et al. 2002), we get $\nu_{\rm m1} \simeq 1.1$ keV. This is smaller than the maximum values that we observe at the limbs. However a relatively small change in the radio slope that we used could alter that. For example moving from 0.6 to 0.57 as in Berezhko et al. (2002) we would obtain a maximum cut-off frequency around 1 keV. Indeed the X to radio ratio that they find in their Fig. 3 is close to 3×10^{-6}, compatible with the peak values we see (Fig. 8).

Our data clearly favors the "polar cap" model for the non-thermal emission. But we are then left with the problem of explaining the obvious large scale asymmetry between southeast and northwest. The most likely reason is a density gradient in the pre supernova gas (northwest is toward the Galactic Plane). However we could not think of a specific reason how this would explain why the non-thermal X-ray emission peaks closer to the northwest side than the radio emission (Sect. 3.1).

5.3. Anisotropy of the synchrotron emission

The arguments above apply rigorously only when the magnetic field is sufficiently disordered behind the shock that the synchrotron emission can be considered isotropic. This is probably not completely true, and the synchrotron emission will be preferentially perpendicular to the $\boldsymbol{B}$ field (because the electrons radiate most and at highest energy when their velocity is perpendicular to $\boldsymbol{B}$). Five points should be considered:

- If the turbulent magnetic field is much smaller than the ordered one, the other limit should be considered (entirely ordered $\boldsymbol{B}$). The result will not change drastically, though, because the azimuthal profile will be non uniform only where the magnetic direction is significantly changed at the shock, i.e. at intermediate latitudes.
- If the field is isotropic just upstream of the gas shock (as might be the case if it is amplified by the cosmic rays themselves), then it is not any longer just downstream. The tangential components are amplified by the compression ratio whereas the radial component is untouched. But this effect will favor the center over the limbs in an equatorial model, because the two directions perpendicular to the line of sight at the equator are both tangential at the center, whereas only one of them is at the limbs.
- Polarisation studies (Reynolds & Gilmore 1993) indicate that the field is preferentially radial. If that was true over the whole sphere, that geometry could indeed reduce and soften the emission toward us in the center, explaining the observed lack of X-ray emission there even in an equatorial geometry. However we would then have to explain how an initially tangential field becomes radial behind the shock. Our feeling is that this interpretation raises more issues than it solves. Also the data is significant only in the bright limbs themselves (where $\boldsymbol{B}$ is indeed radial in the polar cap model) and the modest polarisation fraction suggests that the ordered field does not dominate.
- In the polar cap model, the anisotropy of the synchrotron emission would also be important if the ordered field dominates. It would reduce the emission of those remnants where $\boldsymbol{B}$ is directed toward us, and make them less center-filled.
- Radiative losses (important when the field is large) do not affect the angular distribution because the diffusion isotropizes the electrons faster than they lose energy.

The observed value of $\mathcal{R}_{\pi/3}$ (Sect. 3.2) is far enough below the theoretical limit for isotropic emission to make the result robust to that complication.

Acknowledgements. J.B. wishes to thank D. Ellison for enlightening discussions about particle acceleration in an oblique magnetic field. G.D. is grateful to S. Mader for carrying out the observations at Parkes Observatory and for his help in the initial processing of the Parkes data. She acknowledges G. Castelletti's help in the radio data processing. We are grateful to the referee, R. Bandiera, for helpful comments and spotting an important mistake in one formula. Part of the project was supported by the CONICET (Argentina) - CNRS (France) cooperative science program No. 10038.

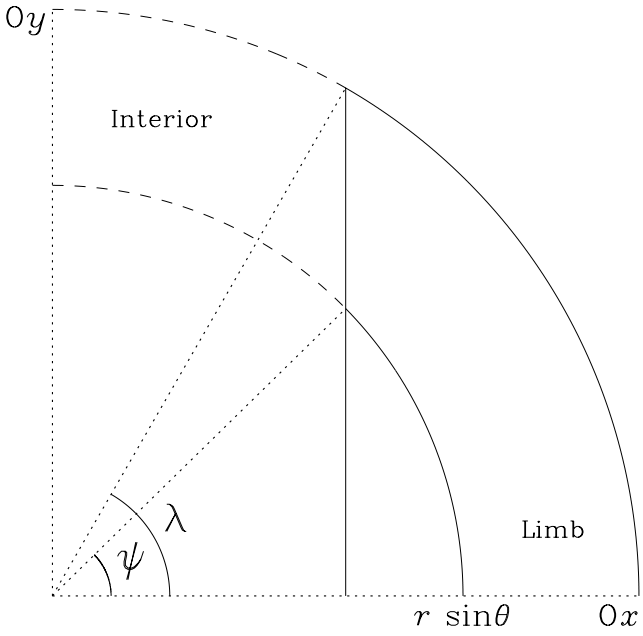

Fig. A.1. Geometry considered in Appendix A. The symmetry axis Oz is perpendicular to the plane of the figure. Only one quarter is shown (the geometry is symmetric with respect to both axes).

Appendix A: Projection of an axisymmetric model

A.1. Definitions

Let us consider an axisymmetric source of isotropic radiation within a sphere of radius unity. In any energy band, the emissivity $\mathcal{P}(r, \theta)$ depends only on radius r ($0 \leq r \leq 1$) and polar angle θ ($0 \leq \theta \leq \pi$). We call Oz the symmetry axis, and Ox the perpendicular axis which is contained in the plane of the sky. The emissivity projected onto Ox (the transverse profile) obviously does not depend on the angle between the symmetry axis and the line of sight. For simplicity, we compute it when Oz is along the line of sight. We split the remnant into two parts, defined by an opening angle λ (Fig. A.1): the interior at $|x| < \cos\lambda$ (which includes the southeast and northwest edges in the case of SN 1006), and the limbs at $|x| > \cos\lambda$. We define $\mathcal{R}_\lambda$ as the ratio between the total power coming from the center and that coming from the limbs.

A.2. Minimum ratio

In projection onto the plane of the sky, any annulus defined by r and θ is either entirely in the interior (if $r\sin\theta < \cos\lambda$) or intersects the $x = \cos\lambda$ line at an angle ψ such that $r\sin\theta\cos\psi = \cos\lambda$. The ratio $\mathcal{R}_\lambda(\psi)$ for that particular annulus is directly the ratio of the angular sectors $(\pi/2 - \psi)/\psi = \pi/(2\psi) - 1$. Because $r \leq 1$, $\psi \leq \lambda$ so that $\mathcal{R}_\lambda(\psi) > \pi/(2\lambda) - 1$.

The total $\mathcal{R}_\lambda$ (averaged over all annuli) will also always be larger than that absolute minimum. $\mathcal{R}_\lambda > \pi/(2\lambda) - 1$. The minimum is reached when the emission is concentrated in a wire circling the equator ($r\sin\theta = 1$). Any broader distribution of the emission (either in latitude or in radius) can only increase that ratio.

In Sect. 3.2 we have chosen to test $\mathcal{R}_\lambda$ for $\lambda = \pi/3 (\cos\lambda = 0.5)$. This is a simple angle which visually encompasses the bright limbs (Fig. 2, bottom left). We expect $\mathcal{R}_{\pi/3} > 0.5$.

References

Arnaud, M., Majerowicz, S., Lumb, D., et al. 2002, A&A, 390, 27
Bamba, A., Yamazaki, R., Ueno, M., & Koyama, K. 2003, ApJ, 589, 827
Baring, M. G., Ellison, D. C., Reynolds, S. P., Grenier, I. A., & Goret, P. 1999, ApJ, 513, 311
Berezhko, E. G., Ksenofontov, L. T., & Völk, H. J. 2002, A&A, 395, 943
Berezhko, E. G., Ksenofontov, L. T., & Völk, H. J. 2003, A&A, 412, L11
Berezhko, E. G., & Völk, H. 1997, Astropart. Phys., 7, 183
Blandford, R. D., & Eichler, D. 1987, Phys. Rept., 154, 1
Dubner, G. M., Giacani, E. B., Goss, W. M., Green, A. J., & Nyman, L. A. 2002, A&A, 387, 1047
Dyer, K. K., Reynolds, S. P., Borkowski, K. J., Allen, G. E., & Petre, R. 2001, ApJ, 551, 439
Dyer, K. K., Reynolds, S. P., & Borkowski, K. J. 2004, ApJ, 600, 752
Ellison, D. C., Baring, M. G., & Jones, F. C. 1995, ApJ, 453, 873
Ellison, D. C., Berezhko, E. G., & Baring, M. G. 2000, ApJ, 540, 292
Fulbright, M. S., & Reynolds, S. P. 1990, ApJ, 357, 591
Ghavamian, P., Winkler, P. F., Raymond, J. C., & Long, K. S. 2002, ApJ, 572, 888
Hendrick, S. P., & Reynolds, S. P. 2001, ApJ, 559, 903
Jokipii, J. R. 1987, ApJ, 313, 842
Koyama, K., Petre, R., Gotthelf, E. V., et al. 1995, Nature, 378, 255
Lagage, P. O., & Cesarsky, C. 1983, A&A, 125, 249
Long, K. S., Reynolds, S. P., Raymond, J. C., et al. 2003, ApJ, 586, 1162
Moffett, D. A., Goss, W. M., & Reynolds, S. P. 1993, AJ, 106, 1566
Read, A. M., & Ponman, T. J. 2003, A&A, 409, 395
Reynolds, S. P. 1996, ApJ, 459, L13
Reynolds, S. P. 1998, ApJ, 493, 375
Reynolds, S. P., & Ellison, D. C. 1992, ApJ, 399, L75
Reynolds, S. P., & Gilmore, D. M. 1986, AJ, 92, 1138
Reynolds, S. P., & Gilmore, D. M. 1993, AJ, 106, 272
Reynolds, S. P., & Keohane, J. W. 1999, ApJ, 525, 368
Roger, R. S., Milne, D. K., Kesteven, M. J., Wellington, K. J., & Haynes, R. F. 1988, ApJ, 332, 940
Tanimori, T., Hayami, Y., Kamei, S., et al. 1998, ApJ, 497, L25
Turner, M. J. L., Abbey, A., Arnaud, M., et al. 2001, A&A, 365, L27
Vink, J., Laming, J. M., Gu, M. F., Rasmussen, A., & Kaastra, J. S. 2003, ApJ, 587, L31
Völk, H. J., Berezhko, E. G., & Ksenofontov, L. T. 2003, A&A, 409, 563
Willingale, R., West, R. G., Pye, J. P., & Stewart, G. C. 1996, MNRAS, 278, 749
Winkler, P. F., & Long, K. S. 1997, ApJ, 491, 829
Winkler, P. F., Gupta, G., & Long, K. S. 2003, ApJ, 585, 324